RSC Advances

PAPER

View Article Online
View Journal | View Issue

Cite this: *RSC Adv.*, 2023, **13**, 16559

Ordered growth of metal oxides in patterned multi-angle microstructures†

Zhenkai Ji,[abc] Min Sun,[a] Tiantian Chen,[a] Xinyi Shen,[a] Xiuzhen Xu,[a] Yan Zhong,[d] Dadong Wang,[d] Jiwei Ma,[a] Bo Chen,*[a] Zhiguo Yi[bc] and Xiaobin Xu*[a]

Herein, we report a facile method combining top-down patterning transfer and bottom-up nanorod growth for preparing large-area and ordered TiO_2 nanorod arrays. Pre-crystallization seeding was patterned with nanostructured morphologies *via* interfacial tension-driven precursor solution scattering on various types and period templates. This is a widely applicable strategy for capillary force-driven interfacial patterns, which also shows great operability in complex substrate morphologies with multiple-angle mixing. Moreover, the customized patterned lithographic templates containing English words, Arabic numerals, and Chinese characters are used to verify the applicability and controllability of this hybrid method. In general, our work provides a versatile strategy for the low-cost and facile preparation of hydrothermally growable metal oxide (*e.g.*, ZnO and MnO_2) nanostructures with potential applications in the fields of microelectronic devices, photoelectric devices, energy storage, and photocatalysis.

Received 3rd March 2023
Accepted 13th May 2023

DOI: 10.1039/d3ra01423a

rsc.li/rsc-advances

1. Introduction

Micro & nano technology (MNT) refers to the design, processing, system integration and application technology of components with micron, sub-micron, and nanometer scales in its constituent systems, which also involve multidisciplinary and multi-disciplinary intersections.[1] It is generally accepted that micron-scale processing refers to the fabrication of tiny structures of 0.1–100 μm in size, while 0.1–1 μm is commonly referred to as the submicron range. Nanoscale processing refers to the process of producing tiny structures of 1–100 nm in size. In the past decades, MNT has been rapidly developed to the nano-level for fine regulation of material properties. In detail, the facile and unconstrained patterning processes are necessary when it comes to device applications, such as microelectronic devices[2,3] and semiconductor components.[4] Among them, additive or subtractive manufacturing-based fabrication techniques such as mechanical micromachining,[5] laser direct writing,[6] photolithography,[7] epitaxial growth,[8] and transfer printing[9] play an important role in device integration. In particular, photolithography is a simple and low-cost method for large-scale preparation and plays a key role in the field of MNT processing.

Titanium dioxide (TiO_2) is a typical n-type semiconductor material with a band gap of 3.0–3.2 eV.[10] It is an abundant, non-toxic and chemically stable material with excellent optoelectronic properties and outstanding semiconductor properties. A variety of TiO_2 nanostructures, including nanoparticles,[11] nanorods,[12,13] nanowires,[14] nanotubes,[15] and nanosheets,[16] play a great role in photocatalysis,[17] solar cells,[18] ion batteries,[19] supercapacitors,[20] photochemical sensors,[21,22] biomedical applications,[23] and other applications. The traditional methods for fabricating TiO_2 nanostructures include electrochemical deposition,[24] chemical vapor deposition,[25] template method,[26] hydrothermal treatment,[27] and sol–gel method.[28] The hydrothermal method is a simple, economical, and high-yield bottom-up method for growing single-crystal TiO_2 nanorods. The TiO_2 nanorod grown by hydrothermal epitaxial are characterized by high crystallinity, controllable size and uniform morphology, but the TiO_2 nanorod fabricated by this method have certain limitations, *i.e.*, the grain size distribution, major crystalline phase orientation and surface growth sites are rather random. This makes it impossible for traditional hydrothermal methods to fabricate ordered patterned TiO_2 nanostructures for more complex applications, such as nano-components,[29] microelectronic devices and integrated fabrication.[30,31]

As a traditional top-down patterning method for different materials, lithography is widely used in the semiconductor industry. When directly applied to rigid materials, such approaches usually have the disadvantage of high cost, as they

[a]*Key Laboratory of Advanced Civil Engineering Materials of Ministry of Education, Shanghai. Key Lab. of D&A for Metal-Functional Materials, School of Materials Science & Engineering, Institute for Advanced Study, Tongji University, Shanghai 201804, China. E-mail: xiaobinxu@tongji.edu.cn; bo.chen@tongji.edu.cn*

[b]*State Key Laboratory of High-Performance Ceramics and Superfine Microstructure, Shanghai Institute of Ceramics, Chinese Academy of Sciences, Shanghai 200050, China*

[c]*University of Chinese Academy of Sciences, Beijing 100049, China*

[d]*Shanghai Highway Investment Construction and Development Co., Ltd., Shanghai 200336, China*

† Electronic supplementary information (ESI) available. See DOI: https://doi.org/10.1039/d3ra01423a

either require expensive equipment or have low flux.[32] Therefore, they are not suitable for the scalable patterning applications of metal oxide crystals. One strategy to address this challenge is to develop a hybrid method,[33–35] *i.e.*, a combination of a top-down pattern transfer method and a bottom-up nanomaterial growth method,[36–39] that is capable of forming arbitrary patterns. J. Volk's group[40] successfully prepared vertically aligned hexagonal ZnO nanorod arrays by using polystyrene nanospheres as a mask for lithography. Rusen Yang's group[41] developed a vertical ZnO nanowire array grown on a flexible polyethylene terephthalate substrate based on a hydrothermal method, which was applied to strain sensors with high stability and fast response time.

In this work, we report a hybrid approach combining top-down and bottom-up processes to prepare patterned arrays of large-area and ordered TiO_2 nanostructures by directionally dispersing the spin-coated precursor on the template surface, and hydrothermal growth treatment of the shaped nucleated crystalline seed layer. The seed layer molding can be applied in a variety of micro/nano structure templates, such as linear, mesh, and inverted pyramid, as well as a wide range of angle types, including acute, right angle, and obtuse angle. In addition, the effects of the growth temperature, duration and reaction concentration on the structural morphology of the TiO_2 nanorods are investigated, and the controlled growth of the TiO_2 nanorod in terms of the crystal morphology, structural sparsity and cluster orientation are achieved at pre-designed positions. This work makes three-dimensional patterned nanomaterial arrays more convenient and accessible, *i.e.*, homogeneous and ordered metal oxide (*e.g.*, ZnO and MnO_2) nanostructure arrays with potential applications in the fields of optoelectronics,[42,43] energy storage,[44] catalysis,[45–47] and biomedicine.[48–51]

2. Experimental section/method

2.1. Materials

The self-designed hard mask was customized from Xi'an Boyan Micro-Nano International Technology Co., Ltd. (China); the silicon oxide wafers (P100) of ~700 μm were purchased from Suzhou Crystal Silicon Electronics & Technology Co., Ltd. (China); the positive photoresist HTI-751, negative photoresist SUN-9i and ZX-238 developer were acquired from Suzhou Research Materials Microtech Co., Ltd. (China); the specialty gases of the preparation process were from Shanghai Xiangkun Special Gas Co., Ltd.; anhydrous potassium hydroxide (KOH) was purchased from Shanghai Aladdin Biochemical Technology, Co., Ltd. (China); all of the chemicals without special declaration were obtained from Sinopharm Group Corp. (China).

2.2. Fabrication devices

The P15 O_2-gas plasma dry cleaner and 280 reactive ion etching (RIE) machine were purchased from Hefei Poly Vacuum Science and Technology, Ltd. (China); The 12A spin-processor was from Zhangqiu Guanpai Electronic Equipment Factory (China); the SX2 electric box resistance furnace was obtained from Shaoxing Shangyu Daoxu Kexi Instrument Factory (China); the DHG-9 benchtop electric constant temperature blast oven was customized from Shanghai Yiheng Technology Instrument Co., Ltd. (China); the hydrothermal reactor was from Xi'an Yibeier Instrument Equipment Co., Ltd. (China). The WH220 heated magnetic agitator was from Wiggens Technology (Beijing) Co., Ltd.

2.3. The fabrication of SiO_2 templates with nanostructure arrays

Before the fabrication of the nanostructure templates, the cut-out SiO_2/Si (P100) (SiO_2 at ~100 nm thickness, Si at ~600 nm thickness) wafer processed in a Teflon flower basket with the piranha solution or organic solvents was ultrasonically treated for 60 min. After blow-drying with the gas gun, the wafer was processed in an O_2 plasma device (cavity pressure: 10–20 Pa, work power: 100–150 W, and work time: 120–180 s). The photoresist was coated through a spin-processor to form a uniform film on the surface of the silicon oxide substrate (spin-coat conditions: 2000 rpm for 40 s). Then, using the ultraviolet lithography machine to expose, the pattern was transformed from the hard mask to photoresist. After development, the periodic nano-pattern arrays of the SiO_2 substrate were presented, and a post-bake process was used to increase the etching resistance of the photoresist. The periodic nano-pattern of the photoresist film was transferred to the SiO_2 layer through the dry etching treatment (gas composition: $CHF_3 : CF_4 = 1 : 1$ in volume, cavity pressure: 15 Pa, work power: 300 W, etching time: 10 min). The residual photoresist was taken down from the substrate *via* the removal immersion. With the protection of the surface SiO_2, the pre-design morphology of the Si wafer was formed under KOH-anisotropic etching. The deionized water was employed for removing the residual alkali of the surface substrate, and the remaining SiO_2 layer was dissolved in diluted HF solution (5–10% aq.) for immersion for 10 min. A ~100 nm thick SiO_2 film was uniformly thermally grown on the silicon nano-pattern substrate *via* a period of calcination in a muffle furnace.

2.4. TiO_2 seeding precursors

A certain amount of TiO_2 seed precursor was prepared. A total volume of 1.0 mL concentrated HCl (AR, ~30% aq., Sigma Aldrich) was mixed with 25.0 mL of isopropanol (AR 99%, Sigma Aldrich) for rotating at 1000 rpm for 30 min in room temperature. Varied amounts of tetra-*n*-butyl titanate ($C_{16}H_{36}O_4Ti$, 99%, Sigma Aldrich) were added slowly to the mixture under rotation. The solution was then stored in the reagent refrigerator for later use.

2.5. TiO_2 growth precursors

The TiO_2 nanorod precursor solution was fabricated using similar methods. A volume of 120 mL hydrochloric acid (30% aq.) and 120 mL isopropanol were mixed and rotated at 1000 rpm for 30 min. An amount of tetra-*n*-butyl titanate was added slowly to the mixture using a pipette gun (4 M: add 4 mL tetra-*n*-butyl titanate). The solution was stored in the reagent refrigerator for later use.

2.6. Capillary force assisted nucleation of TiO_2 on the nanostructure arrays

In order to realize the capillary force-assisted TiO_2 seeding precursors controlled nucleation, a homogeneous spin-coating strategy was adopted to disperse the dilute mixture solution. The silicon oxide substrate with nanostructure array was treated by plasma cleaner (gas: high-purity O_2, cavity pressure: 15–20 Pa, work power: 100 W, and treatment time: 180 s) to increase the surface hydrophilicity. A volume of 200 μL of the seeds precursor solution was dropped onto the SiO_2 template, and then a spin-coating process (3500 rpm for 40 s) was performed to remove excess solvent. The SiO_2 templates were heated on a plate heater at 150 °C under normal atmosphere for 5 min. In the process of heating and concentration, the seed precursor solution gradually formed the solid–liquid mixed phase of precrystallization. The mixture with mobility wets the micro–nano structure template, and is uniformly distributed at the corresponding angles by means of capillary forces. For crystallizing the TiO_2 seeds nucleation in the pre-selected area and enhancing the interfacial bonding force, the SiO_2 template with nanostructure arrays covered with TiO_2 seeds was calcined in a muffle furnace at 600 °C for 120 min.

2.7. Pattern growth of the TiO_2 nanorod arrays

Firstly, the SiO_2 nanostructure arrays template coated with TiO_2 seed should be prepared by spin-coat process and calcination treatment according to experimental requirements. Then, ~20 mL as-prepared TiO_2 growth precursor solution was transferred into a 50 mL Teflon high-temperature reactor, in which the reaction template base had been pre-placed. The high-temperature reactors were placed in the pre-heated electric oven at 140–200 °C for a certain amount of time. After the reaction was cooled to room temperature, the products were separated carefully from the Teflon container. The substrate was washed with deionized water and absolute ethanol three times, then heated at 450 °C for 1 h to remove the surface organic attachment. When the muffle furnace was cooled, the pattern-grown TiO_2 nanorod arrays were prepared for subsequent characterization.

2.8. Materials characterizations

Scanning electron microscopy (SEM) images of the microscale morphology were obtained on a Zeiss Sigma 300 VP operated at 0–20 kV. At room temperature, the X-ray diffraction (XRD) data were collected through a Bruker D8 Advance powder diffractometer (operating at 40 kV, 40 mA, a Cu-Kα source) fitted with a beryllium window.

3. Results and discussions

3.1. Preparation of TiO_2 nanorod arrays on patterned substrates

The patterned TiO_2 nanorod arrays were fabricated by the combined top-down and bottom-up approaches, the major tenets of which are shown in Scheme 1. The pre-designed templates were obtained by traditional top-down processes, *e.g.*, ultra-violet (UV) lithography, RIE process, and wet etching techniques. The patterned TiO_2 nanorod arrays were then fabricated on the prepared templates by the bottom-up process, including solution crystallization precipitation and *in situ* thermal growth.

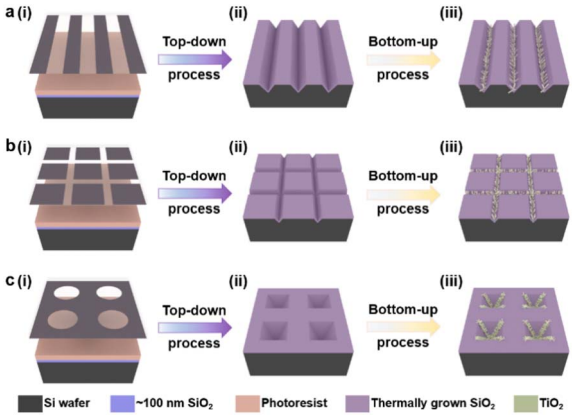

Scheme 1 The fabrication scheme of the TiO_2 nanorod arrays *via* top-down (photolithography) and bottom-up (hydrothermal growth) methods in various templates. The linear template is prepared *via* photolithography by transferring the pattern from a hard mask to silicon substrate; the region-selective linear TiO_2 nanorod arrays are generated by thermal growth of coated seeds. (a) The linear template. (b) The mesh template. (c) The pyramidal template.

The lithography hardmask was designed based on the preliminary results that had been explored, and the processing and preparation were entrusted to the qualified related enterprises. A cleaning surface facilitates the formation of uniform and stable photoresist films during the lithography process. Thus, the cleaning process is a necessary precondition for the promising UV-lithography process in SiO_2–Si wafers. During this process, the combination of piranha solution, organic cleaning solvents, ultrasonic washing, and oxygen-plasma cleaning is used. In Fig. 1, a layer of photoresist is spin-coated onto a clean SiO_2–Si wafer, and the photoresist is dried on a heated plate at 90 °C for 60 s. UV exposure is then performed with a photolithograph to produce a photoresist film containing the transfer pattern. The unprotected SiO_2 was eliminated *via* the dry etching process. Thus, the periodic pattern is further transferred to the SiO_2 layer. Regular arrays of nanostructures are produced on the Si substrate by anisotropic wet-etching under the protection of the SiO_2 hard-mask. After removing the surface alkaline and residual SiO_2, the substrates are calcined in a muffle furnace for oxidizing in an external-to-internal manner. Finally, a SiO_2 template capable of growing a nanorod is formed. As shown in Fig. 1a(v)–c(v), the linear template, the pyramidal template and the mesh template are fabricated using similar approaches. These included angles generated by the substrate microstructure are quite different, such as ~70° for V-shaped nanowires, ~110° for inverted nanopyramids, and ~90° for network structures. This angle is designed based on the intrinsic crystalline phase and nanostructure morphology of the silicon wafers, which is influenced by macroscopic wet-etching conditions, etchant type, reaction

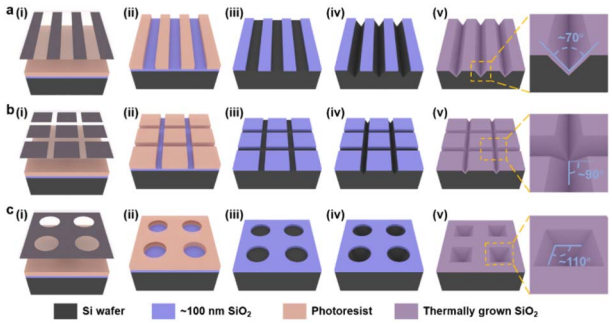

Fig. 1 The detailed schematic for developing the different substrate templates using the traditional top-down approaches. (a) The linear template. (b) The mesh template. (c) The pyramidal template. (i) Photolithography is used to transfer the pattern from the hard mask to the photoresist on the silicon substrate through ultraviolet light. (ii) After developing, the patterned photoresist is formed on the silicon wafer. (iii) Under the protection of the patterned photoresist, the dry-etching machine is used to corrode the exposed SiO_2 film. (iv) After a period of reaction in a hot alkaline solution, anisotropic etching occurs on the exposed surface of the silicon wafer to produce the target morphology. (v) The substrate is cleaned and calcined in a muffle furnace, and then the SiO_2–Si template is formed.

temperature, etching solution concentration, and others. Although there were inevitable errors between the actual preparation process and the ideal templates, a series of templates with different styles of angle were still prepared with sufficient experience, including acute angle, right angle, and obtuse angle.

3.2. The growth regulation of TiO_2 nanorod arrays

As illustrated in Fig. 2a, the bottom-up nanorod growth strategy consists of two components: crystal seed forming and nanorod *in situ* growth. Both are critical for the microscopic morphology of the SiO_2–Si template. For this multi-influence factors problem, the orthogonal decomposition and univariate control method is used. Firstly, the linear template was selected for an intensive study of crystal seed formation because of its relatively simple morphology. After the pre-spin coating, a finite precursor solution is formed in the surface microstructure of the linear template. The volume of the solution decreases gradually during the process of heating and concentration, and the precipitated crystals are evenly distributed in the bottom of the V-shaped groove under the action of capillary force, and a patterned crystalline seed layer is formed in Fig. 2a(ii). The SEM images of the crystalline morphology, corresponding to different precursor solution concentrations, are presented in Fig. 2b. With the increase of TiO_2 precursor content in the mixture, the effective volume of nucleated seeds in the patterned nanoarray increased. It can be found from the SEM images that the volume occupied by the seeds in the V-groove increases, the bottom surface of the inverted trapezoidal slot increases, and the depth decreases. Even though these three kinds of seed layers are reacted under the same thermal growth conditions, significant differences in nanorod morphology are shown. In practical application, it is observed that the seed layer formed by 0.001 M concentration precursor is smaller in size with a smaller contact area with the substrate after nucleation and a weaker bonding strength. Especially under high temperature and pressure conditions, the seed layer separation is easily separated from the substrate. The nanorod might fall off or grow chaotically in some regions, destroying the whole homogeneity and regioselective of the TiO_2 nanorod. The seed layer formed by the 0.01 M concentration precursor has a larger contact area with the substrate and stronger bonding strength after nucleation. However, the seed precipitation formed during high-temperature calcination is not the major crystalline phase of the hydrothermally grown nanorod, and the excessive seed layer will reduce the crystallinity of the nanorod in the template. A related phenomenon has been reported in fundamental studies.[52,53] As shown in the linear template of Fig. S1(i),† the initial nanorod growth location is the edge of the crystallized seed layer. More obvious contrast results are observed in the inverted pyramidal template in Fig. S1(ii).† Therefore, the ~0.003 M concentration solution precipitates crystals with less differential impact to form the seed layer during the drying process, which makes it a great choice to continue the morphological investigation.

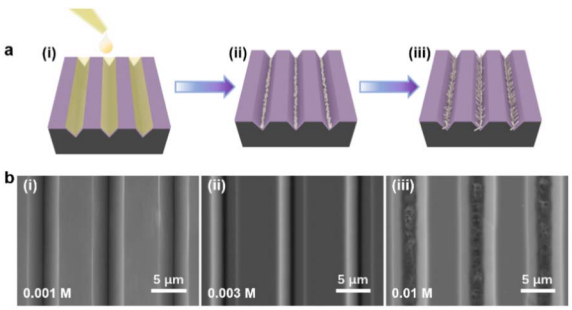

Fig. 2 (a) The detailed scheme is shown employing the conventional bottom-up approach for TiO_2 nanorod growth in substrate templates. (i) The pre-fabricated TiO_2 seed solution is spin-coated on the SiO_2–Si template. (ii) The dispersed solution precipitates crystals in the drying process, and forms a seed layer. (iii) The linear TiO_2 nanorod arrays were hydrothermally growing on the crystalline seed. (b) SEM images of the morphological changes of the TiO_2 crystalline seeds after drying treatment at different precursor concentrations. Scale bars: 5 μm.

The TiO_2 hydrothermal process occurring in the precursor solution can be described by the hydrolysis reaction of tetrabutyl titanate and the condensation reaction of the titanium intermediates.[54] The TiO_2 nanostructure morphology of conventional hydrothermal treatment involves a variety of factors, including growth period, heating temperature, and reaction concentration.[55,56] We have investigated the effects of these conditions on the morphological evolution of TiO_2 growth processes through a single control variable approach to obtain TiO_2 nanorod arrays with controllable morphology, easy preparation, and high reproducibility. In Fig. 3a, the typical SEM images of the TiO_2 nanorod array are obtained on the linear template at different reaction times from 0.5 h to 3 h. The average size of the nanorod obtained at different times is measured and summarized in Fig. 4a. With increasing reaction time, the lengths and diameters of the nanorod increase from

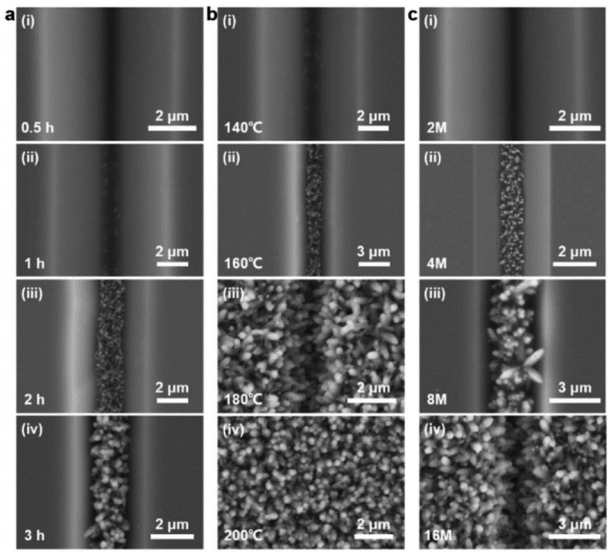

Fig. 3 (a) SEM images of the TiO_2 nanorod arrays grown at different reaction times: (i) 0.5 h, (ii) 1 h, (iii) 2 h, and (iv) 3 h (temperature: 170 °C, concentration: 4 M). (b) SEM images of the temperature-dependent growth of TiO_2 nanorod arrays. (i) 140 °C, (ii) 160 °C, (iii) 180 °C, and (iv) 200 °C (time: 2 h, concentration: 4 M). (c) SEM images of the TiO_2 nanorod arrays according to different reactant concentrations. (i) 2 M, (ii) 4 M, (iii) 8 M, and (iv) 16 M (time: 2 h, temperature: 170 °C).

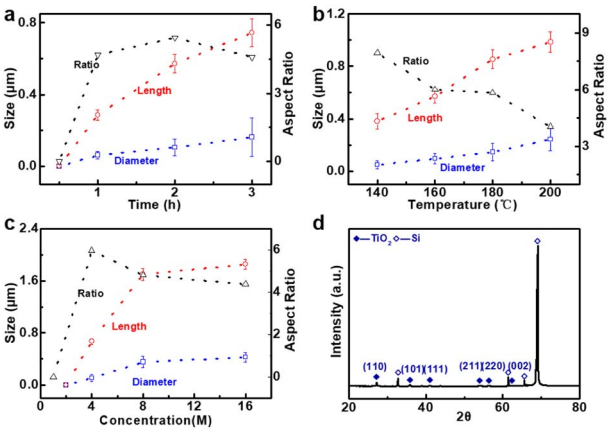

Fig. 4 (a–c) Statistical schematic of the average diameters, lengths and aspect ratio of the TiO_2 nanorod under different reaction conditions: (a) time, (b) temperature, (c) concentration. (d) The XRD data of the TiO_2 nanorod arrays on the linear template substrate (template is ~5 μm groove and 10 μm arrays period. Scale bar marked in the figure).

unmeasurably small sizes to ~0.743 μm and ~0.162 μm, respectively. The results show that the beginning stage of the hydrothermal reaction is dominated by TiO_2 nanocrystal formation, and the size of the nanorods increases over a long period of time. The dependence of the morphological evolution of the TiO_2 nanorod on the reaction temperature is shown in Fig. 3b and 4b. As the reaction temperature increases, the length and diameter of the nanorod increase from ~0.381 μm and ~0.048 μm to ~0.985 μm and ~0.244 μm, respectively. A small number of micro-sized TiO_2 nanorods are formed under a low growth temperature of 140 °C, indicating that a reaction temperature higher than 140 °C is required to obtain large-scale TiO_2 nanorods with limited reaction time. At the same time, if the reaction temperature is too high, the substrate surface morphology will be ignored with limited reaction time (2 h), *i.e.*, the TiO_2 nanorod will spread over the whole substrate and even fill the surface gap of the substrate microstructure to form a plane TiO_2 film (Fig. 3b). According to the SEM data in Fig. 3c and the statistical result in Fig. 4c, it is obvious that the rapid growth mutation of the TiO_2 nanorods slows down after the mass concentration of the growth precursors exceeds 8 M, and the size is maintained at ~2 μm length and ~0.5 μm diameter. We have characterized the typical crystal structures prepared by XRD analysis. The XRD results in Fig. 4d demonstrate that the as-prepared TiO_2 is the rutile phase,[57] *i.e.*, the characteristic peaks in the XRD spectra can be attributed to the TiO_2 (110), (101), (111), (211) and (220) crystal planes. In summary, TiO_2 nanorod arrays with ideal size, reasonable density, and directional distribution can be easily obtained by simply adjusting the hydrothermal temperature, growth time, and reaction precursor concentration.

Based on the experimental results of the morphology control of the TiO_2 nanorods in pre-prepared templates, we have applied them in different sizes of linear templates, and found that they showed excellent applicability and stability. Fig. 5a shows the SEM images of the TiO_2 nanorods employed in the linear templates ranging from a few micrometers to dozens of

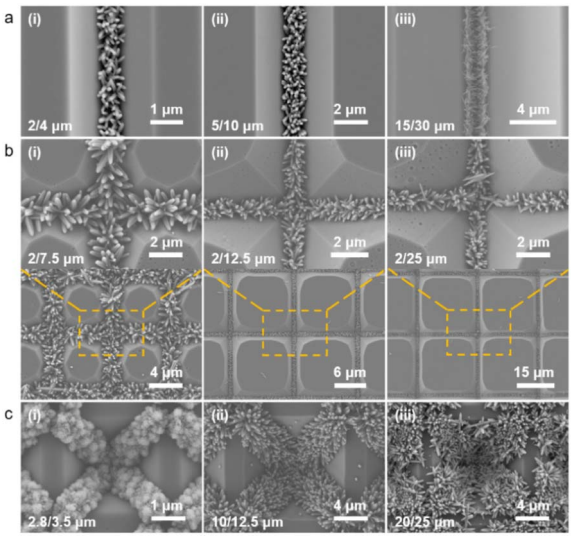

Fig. 5 (a) SEM images of the TiO_2 nanorod arrays in linear templates with different periods: (i) ~2 μm V-shaped groove, 4 μm template cycle. (ii) ~5 μm V-shaped groove, 10 μm template cycle. (iii) ~15 μm V-shaped groove, 30 μm template cycle. (b) SEM images of the TiO_2 nanorod arrays in mesh templates with different periods: (i) ~2 μm mesh lines, 7.5 μm template cycle. (ii) ~2 μm mesh lines, 12.5 μm template cycle. (iii) ~2 μm mesh lines, 25 μm template cycle (detail enlargement at the top). (c) SEM images of the TiO_2 nanorod arrays in pyramidal templates with different periods: (i) ~2.8 μm inverted pyramid, 3.5 μm template cycle. (ii) ~10 μm inverted pyramid, 12.5 μm template cycle. (iii) ~20 μm inverted pyramid, 25 μm template cycle (scale bar marked in the figure).

micrometers. When the microstructure is formed at a sharp angle, the capillary force can play a full role in template with different sizes, resulting in directional and continuous nucleation of the precursor to create a crystal seed layer. The seed site for the subsequent thermal growth can be employed to form a tunably controlled, continuous and homogeneous array of TiO_2 nanorods. If the linear template is treated as a one-dimensional (1D) template, we expand the template dimension to form a planar two-dimensional (2D) mesh template and a three-dimensional (3D) inverted pyramid template, and attempt to introduce the nanorod growth mechanism into them. As shown in Fig. 5b and c, similar results are also exhibited with other types of templates. The seed layer is patterned with the same method; that is, after spinning the coating solution and heating crystallization, the precursor of the solid–liquid mixture phase is evenly distributed along the microstructure angle under the action of capillary force. The SEM images show that in both 2D and 3D templates, the precursor solution crystallizes and nucleates at pre-designed locations, and the TiO_2 nanorod in turn grows directionally along the seed layer distribution to form a patterned nanorod array cluster. Similarly, in substrates with different periods, the 2D and 3D templates also exhibit solution capillary force drive effects, *i.e.*, spin-coated precrystallization can still be applied in nanostructures with right angles or obtuse angles, which significantly enhances the potential application of the method.

Our work has demonstrated that spin-coated precursor solutions can build self-aggregating seed layers in nanostructure substrates with different angles by capillary forces. However, the nanostructure of the multi-angle composite has not been explored, and it is not clear whether there is competition or rejection in it. Therefore, we designed two kinds of composite templates: linear and inverted pyramid. A schematic diagram of the precursor solution self-aggregation, crystalline nucleation, and *in situ* growth of the TiO_2 nanorod in the composite template is shown in Fig. 6a. The preparation process of the composite template is shown in Fig. S2.† It is obvious that the linear composite template is formed without sufficient etching during the wet process to develop an inverted trapezoidal structure with two obtuse angles on both sides of the bottom surface. The toroidal composite template is the original inverted pyramidal model, which has not undergone sufficient etching to form a platform structure, so two different obtuse angles exist. The SEM images of Fig. 6b demonstrate the growth of the TiO_2 nanorod on the linear composite template under different cycles. When the template forms an inverted trapezoidal structure, two similar obtuse angles are present on both sides of the bottom surface. The spin-coated precursor solution spontaneously aggregates on the angle under capillary forces during the drying process, forming a pre-crystallized nanoseed layer. The subsequent TiO_2 nanorod also grows along the pre-crystallized seed layer to fabricate regular shaped and directionally growing nanorod clusters. The SEM images in Fig. 6c demonstrate the growth of the nanorod on the circular composite template at different sizes. The nanorod crystal cluster preparation process is similar to that in the linear composite template, despite some differences in the

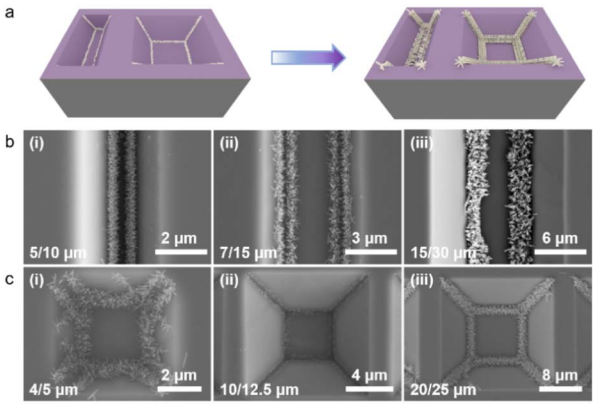

Fig. 6 (a) Schematic diagram of the precursor nucleation and TiO_2 growth in a composite template. (b) SEM images of the TiO_2 nanorod arrays in linear composite templates with different microstructure periods: (i) ~5 μm V-shaped groove with 10 μm template, (ii) ~7 μm V-shaped groove with 15 μm template, (iii) ~15 μm V-shaped groove with 30 μm template. (c) SEM images of the TiO_2 nanorod arrays in toroidal composite templates at different microstructural periods (scale bar marked in the figure).

microscopic morphology. Overall, the difference of the angle position in the linear composite template has no effect on the seed crystallization and nanorod growth; the difference of the angle and position in the ring composite template also has almost no effect on the patterned nanorod growth. The method still shows good compatibility in composite templates.

For further demonstration of the wide applicability and versatility of this hybrid fabrication strategy, we designed and customized patterned lithographic templates containing English words (Fig. 7a), Arabic numerals [Fig. 7b(i)], Chinese characters [Fig. 7b(ii)], and others. After a similar manufacturing process to prepare the available SiO_2–Si template, we successfully achieved arbitrary patterning of TiO_2 nanorod arrays with different characteristics, such as the "NANO", "20", and "Shanghai" characters. This method of capillary force promoting the arbitrary patterning of nanostructures is positive for surface processing of composite materials to device integration of a nano-processed device. We will integrate this approach in our upcoming research for applications in photocatalytic devices, photodetectors, organic–inorganic hybrid cells, super-capacitors, and other devices.

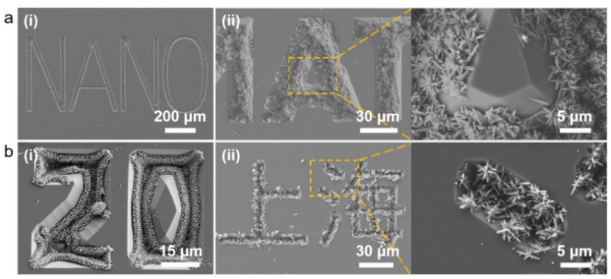

Fig. 7 (a and b) SEM images of the TiO_2 nanorod arrays with different features (scale bar marked in the figure).

4. Conclusions

In summary, we report a hybrid method of micro/nano manufacturing in which a single crystal TiO_2 nanorod array is grown in a multi-type mode substrate to meet the needs of arbitrary patterning. The combination of top-down photolithography and bottom-up hydrothermal treatment provided a simple and facile approach to complex patternization, which is of positive significance for the integration of microelectronic devices. The arbitrary patterns of substrate template are obtained through the lithographic pattern transfer process and wet-etching technology of silicon materials. Under the assistance of capillary force of microstructure angle, a certain amount of TiO_2 seed precursor onto the template surface is gathered in the preset position to form a continuous patterning nucleation during subsequent calcination process. Then, TiO_2 nanorod arrays are grown based on TiO_2 crystallization seeds with various patterns in a controllable manner through conventional hydrothermal treatment. The microscopic morphology and density of the TiO_2 nanorods could be adjusted by controlling the concentration of the seed precursor, hydrothermal reaction time and temperature, and the concentration of growth precursors. In conclusion, this work provides a promising approach to the low-cost and easy preparation of patterned TiO_2 nanorod arrays with potential applications in optoelectronic devices, energy conversion, photocatalysis, and biomedicine in the future.

Author contributions

Z. Ji and M. Sun contributed equally to this work. The experiments were designed by Z. Ji, B. Chen and X. Xu. Data were collected by Z. Ji and M. Sun, and analyzed by all authors. All of the authors contributed to the manuscript writing.

Conflicts of interest

There are no conflicts to declare.

Acknowledgements

This work is financially supported by the National Natural Science Foundation of China (Grant No. 51901159) and the Fundamental Research Funds for the Central Universities.

Notes and references

1 S. Dimov, E. Brousseau, R. Minev and S. Bigot, *Proc. Inst. Mech. Eng., Part C*, 2011, **226**, 3–15.
2 C. Chua, A. Loo and M. Pumera, *Chemistry*, 2016, **22**, 14336–14341.
3 H. Wang, Y. Liu, M. Li, H. Huang, M. Zhong and H. Shen, *Appl. Phys. A*, 2009, **97**, 25–29.
4 C. Chen, Y. Wei, G. Sun and B. Shao, *Chem.–Asian J.*, 2012, **7**, 1018–1025.
5 Y. Yuan, L. Han, D. Huang, J. Su, Z. Tian, Z. Tian and D. Zhan, *Electrochim. Acta*, 2015, **183**, 3–7.
6 S. Gittard and R. Narayan, *Expert Rev. Med. Devices*, 2010, **7**, 343–356.
7 J. Fourkas, *J. Phys. Chem. Lett.*, 2010, **1**, 1221–1227.
8 H. Yu, M. Liao, W. Zhao, G. Liu, X. J. Zhou, Z. Wei, X. Xu, K. Liu, Z. Hu, K. Deng, S. Zhou, J. A. Shi, L. Gu, C. Shen, T. Zhang, L. Du, L. Xie, J. Zhu, W. Chen, R. Yang, D. Shi and G. Zhang, *ACS Nano*, 2017, **11**, 12001–12007.
9 A. Carlson, A. M. Bowen, Y. Huang, R. G. Nuzzo and J. A. Rogers, *Adv. Mater.*, 2012, **24**, 5284–5318.
10 B. Wang, S. Shen and S. S. Mao, *J. Materiomics*, 2017, **3**, 96–111.
11 X. Chen, L. Liu, Z. Liu, M. A. Marcus, W. C. Wang, N. A. Oyler, M. E. Grass, B. Mao, P. A. Glans, P. Y. Yu, J. Guo and S. S. Mao, *Sci. Rep.*, 2013, **3**, 1510.
12 X. Wang, Z. Li, J. Shi and Y. Yu, *Chem. Rev.*, 2014, **114**, 9346–9384.
13 Y. Zhu, L. Yang, J. Sheng, Y. Chen, H. Gu, J. Wei and Z. Zhou, *Adv. Energy Mater.*, 2017, **7**, 1701222.
14 B. Liu, H. M. Chen, C. Liu, S. C. Andrews, C. Hahn and P. Yang, *J. Am. Chem. Soc.*, 2013, **135**, 9995–9998.
15 M. Wang, L. Sun, Z. Lin, J. Cai, K. Xie and C. Lin, *Energy Environ. Sci.*, 2013, **6**, 1211.
16 C. Liu, L. Wang, Y. Tang, S. Luo, Y. Liu, S. Zhang, Y. Zeng and Y. Xu, *Appl. Catal., B*, 2015, **164**, 1–9.
17 Q. Guo, C. Zhou, Z. Ma and X. Yang, *Adv. Mater.*, 2019, **31**, 1901997.
18 B. Roose, S. Pathak and U. Steiner, *Chem. Soc. Rev.*, 2015, **44**, 8326–8349.
19 N. Wang, Z. Bai, Y. Qian and J. Yang, *Adv. Mater.*, 2016, **28**, 4126–4133.
20 H. Zhou and Y. Zhang, *J. Phys. Chem. C*, 2014, **118**, 5626–5636.
21 X. Xu, J. Chen, S. Cai, Z. Long, Y. Zhang, L. Su, S. He, C. Tang, P. Liu, H. Peng and X. Fang, *Adv. Mater.*, 2018, **30**, 1803165.
22 Y. Jing, A. Wang, J. Li, Q. Li, Q. Han, X. Zheng, H. Cao and S. Bai, *Bio-Des. Manuf.*, 2021, **5**, 153–162.
23 K. Mcnamara and S. Tofail, *Adv. Phys.: X*, 2016, **2**, 54–88.
24 G. Li, L. Wu, F. Li, P. Xu, D. Zhang and H. Li, *Nanoscale*, 2013, **5**, 2118–2125.
25 A. Mills, S. K. Lee, A. Lepre, I. P. Parkin and S. A. O'Neill, *Photochem. Photobiol. Sci.*, 2002, **1**, 865–868.
26 G. Zhang, H. B. Wu, T. Song, U. Paik and X. W. Lou, *Angew. Chem., Int. Ed. Engl.*, 2014, **53**, 12590–12593.
27 M. Maria John, K. Ramamurthi, K. Sethuraman and R. Ramesh Babu, *Appl. Surf. Sci.*, 2017, **405**, 195–204.
28 L. Bazli, M. Siavashi and A. Shiravi, *J. Compos. Compd.*, 2019, **1**, 1–12.
29 J. Deng, J. Tao, T. Wu and H. Zhu, *J. Mater. Sci.: Mater. Electron.*, 2011, **23**, 295–301.
30 X. Jiang, Q. Lin, Y. Zhang, K. Dong, Y. Zhang and Y. Shi, *J. Mater. Sci.: Mater. Electron.*, 2017, **28**, 12509–12513.
31 B. Çırak, Z. Demir, Ç. Eden, Y. Erdoğan, B. Caglar, S. Karadeniz, T. Kılınç, A. Ekinci and Ç. Çırak, *J. Mater. Sci.: Mater. Electron.*, 2019, **30**, 6335–6341.
32 P. Fan, M. Zhong, B. Bai, G. Jin and H. Zhang, *RSC Adv.*, 2016, **6**, 45923–45930.

33 L. Yang, D. Chu, L. Wang, G. Ge and H. Sun, *Mater. Lett.*, 2016, **167**, 4–8.
34 G. Kim, T. An and G. Lim, *ACS Appl. Mater. Interfaces*, 2017, **9**, 19057–19062.
35 V. Mehta and S. N. Rath, *Bio-Des. Manuf.*, 2021, **4**, 311–343.
36 X. Wang, Y. Tao, H. Zhao, M. Fu, D. He and Y. Wang, *J. Alloys Compd.*, 2017, **704**, 131–140.
37 L. Liu, Y. Wang, F. Sun, Y. Dai, S. Wang, Y. Bai, L. Li, T. Li, T. Zhang and S. Qin, *Microsyst. Nanoeng.*, 2020, **6**, 31.
38 H. Choi, Y. Lee, J. Yu, K. Hwang and J. Boo, *Materials*, 2016, **9**, 656.
39 Y. Hou, W. Wang and P. Bartolo, *Bio-Des. Manuf.*, 2022, **5**, 556–579.
40 Z. Szabó, J. Volk, E. Fülöp, A. Deák and I. Bársony, *Photon. Nanostruct: Fundam. Appl.*, 2013, **11**, 1–7.
41 W. Zhang, R. Zhu, V. Nguyen and R. Yang, *Sens. Actuators, A*, 2014, **205**, 164–169.
42 Y. Xiong, M. Fang, Q. Zhang, W. Liu, X. Liu, L. Ma and X. Xu, *J. Alloys Compd.*, 2022, **898**, 163003.
43 T. Zhang, Z. U. Rahman, N. Wei, Y. Liu, J. Liang and D. Wang, *Nano Res.*, 2017, **10**, 1021–1032.
44 Z. Bai and Y. Zhang, *J. Solid State Electrochem.*, 2016, **20**, 3499–3505.
45 D. Baiyila, X. Wang, X. Li, B. Sharileaodu, X. Li, L. Xu, Z. Liu, L. Duan and J. Liu, *J. Mater. Chem. A*, 2014, **2**, 12304–12310.
46 J. Xiong, Z. Luo, J. Yang, Y. Guo, A. Piyadasa, S. Wang, S. Hoang, Y. Fang, S. Hu, W. Yang, H. Deng, L. Zhang and P.-X. Gao, *CrystEngComm*, 2019, **21**, 2727–2735.
47 W. Wang, J. Dong, X. Ye, Y. Li, Y. Ma and L. Qi, *Small*, 2016, **12**, 1469–1478.
48 H. Chen, H. Chen, Z. Huang and D. Chen, *Mater. Lett.*, 2014, **124**, 275–278.
49 S. Karim, S. Nadzirah, J. Kazmi, R. Rahim, C. Dee, A. Hamzah and M. Mohamed, *J. Mater. Sci.*, 2021, **56**, 15344–15353.
50 H. Zhou, P. Liu, Z. Gao, Q. Li, W. Lv, J. Yin, B. Zhang, H. Yang and L. Ma, *Bio-Des. Manuf.*, 2022, **5**, 433–436.
51 M. Sun, C. Wang, M. Lv, Z. Fan and J. Du, *J. Am. Chem. Soc.*, 2022, **144**, 7337–7345.
52 J. Wang, Z. Ji, X. Xu, T. Chen, B. Chen, G. Gao, J. Ma, X. Nie and X. Xu, *ACS Omega*, 2022, **7**, 22039–22045.
53 Z. Ji, X. Liu, Y. Song, Y. Zhong, D. Wang, B. Chen, M. Fang, X. Nie, J. Hou, J. Ma, H. Ma, X. Xu, Z. Yi and X. Xu, *J. Colloid Interface Sci.*, 2023, **630**, 436–443.
54 H. Choi, E. Stathatos and D. D. Dionysiou, *Appl. Catal., B*, 2006, **63**, 60–67.
55 M. Maria Angelin Sinthiya, N. Kumaresan, K. Ramamurthi, K. Sethuraman, B. S. Moorthy, B. R. Ramesh and V. Ganesh, *Appl. Surf. Sci.*, 2018, **449**, 122–131.
56 H. Lu, Y. Zhou, S. Vongehr, S. Tang and X. Meng, *Sci. China: Technol. Sci.*, 2012, **55**, 894–902.
57 M. Maddah, C. P. Unsworth and N. O. V. Plank, *Mater. Res. Express*, 2018, **6**, 015905.